Rigid-Foldable Doubly-Curved Deployable Reflectors Based on the Miura-Ori Pattern

Tianshu Wang * and Matthew Santer†
Imperial College London, London, England SW7 2AZ, United Kingdom

This paper introduces a novel deployable reflector concept which achieves single degree-of-freedom folding of solid doubly-curved surfaces ‡. A set of folding kinematics is constructed using the Miura-Ori pattern and the Hoberman linkage to allow compact collision-free stowage of a fully-rigid truss-supported solid-surface reflector structure. In this paper, the baseline kinematic architecture is introduced and a design methodology using Bayesian optimization to systematically obtain optimally-stowed geometries is detailed. An example design is carried out to demonstrate the methodology. Optimal parameters are produced, the design space is explored, and a detailed design based on the optimal parameters is made, along with its derivative variants. Finally, a prototype model and quantification of surface errors confirm the validity of resulting designs.

I. Nomenclature

a	=	Fold angles of the origami pattern
A	=	Cross section area of reflector truss member
C	=	Crease between two vertices of the origami pattern
d_d	=	Reflector structural depth
D_X	=	X dimension of the reflector bounding box
D_Y	=	Y dimension of the reflector bounding box
D_Z	=	Z dimension of the reflector bounding box
E	=	Elastic modulus of reflector material
f	=	Reflector focal length
F	=	Objective function minimized for optimization
i	=	X-direction index of vertices
j	=	Y-direction index of vertices

*Research Postgraduate, Department of Aeronautics. Member AIAA.
†Professor of Aerospace Structures, Department of Aeronautics, m.santer@imperial.ac.uk, Associate Fellow AIAA (Corresponding author).
‡This paper was originally presented as: "A Truss-Supported Doubly-Curved Deployable Reflector Based on the Miura-Ori Pattern", *AIAA SciTech 2024 Forum*, January 2024, Orlando. https://doi.org/10.2514/6.2024-2256.

L = Length of reflector truss member

δL = Length deviation of reflector truss member

n_{col} = Number of collided points in the reflector collision model

N_c = Number of columns in the reflector

N_r = Number of rows in the reflector

P_a = Origami panels on the reflector supporting structure

P_b = Surface panels of the reflector

S = Measure of slant for surface panel alignment

t_p = Reflector panel thickness

V_a = Vertices on the reflector supporting structure

V_b = Vertices on the reflector surface panel

σ_{RMS} = overall surface RMS standard deviation

σ_{single} = standard deviation caused by error from a single truss member

σ_{total} = total standard deviation compounded from multiple truss errors

σ_{truss} = standard deviation of truss length

II. Introduction

Deployable reflectors are useful for reconciling the conflicting requirements for smaller packaged size at launch, and larger operational size after reaching orbit. With the advent of increasingly small satellites and corresponding launch vehicles, there is a practical need for spacecraft components to also decrease in size, but reflector sizes are constrained by physics including Friis' transmission formula [1] for RF applications, and the Rayleigh criterion for optics. Meanwhile, research is striving to achieve larger and better reflectors, both for optics, like the James Webb Space Telescope [2], and for various RF applications [3, 4]. Apart from size, reflector surface precision is also important. Ruze's equation [5] quantifies the effect of RMS surface precision on RF reflector gain. The required surface precision is proportional to operating wavelength. Challenges such as bandwidth congestion and demand for higher throughput drive communications to increasingly high frequencies [6], and this leads to the requirement for higher RF reflector surface precision, towards sub-millimeter scale. Optical reflectors require even higher precision, at the micrometer to nanometer scale. Such precision requirements are especially challenging for deployable reflectors, where the compliance or articulation necessary for deployment inevitably introduce larger shape errors than comparable fixed reflector designs.

Numerous deployable reflector solutions exist, each with strengths and weaknesses regarding the aforementioned requirements and challenges. Some examples include mesh-surface reflectors such as the large-scale Astromesh [7] and small-scale RainCube [8], solid-surface reflectors using origami [9] or petal-type [10, 11] deployment, as well as

various reflectors with semi-compliant surfaces[12–14].

This paper focuses on origami-based rigid-foldable reflectors, which carry some unique technical advantages. Using inspiration from origami patterns, mechanically-hinged architectures can be designed to compactly fold fully-rigid components. Surface precision and stowed size of such designs are expected to be between that of typical flexible-surface and typical rigid-surface deployable reflectors. As strain-free deployment is achieved, components can be as stiff as required, so that external loads will lead to smaller deformation. Also, rigid components and mechanical articulation can typically be fabricated more precisely than their flexible counterparts. This all leads to high reflector surface precision. Compared to flexible-surface reflectors such as meshes and inflatable antennas, the concept here alleviates common form-finding challenges. In addition, solid surfaces are more compatible to higher frequencies where meshes would need to be increasingly fine-knit, as well as optics applications. On the other hand, while rigid designs using mechanical articulation lend well to flat surfaces such as solar panels and phased array antennas, design possibilities are more restricted when strain-free folding for double curvature is pursued. This challenge is discussed in [15], which provides one novel way of preserving rigid foldability under curvature. Current solutions also include petal-type folding and the James Webb Space Telescope main mirror folding. The concept here is another approach for solving the problem. To realize the benefits of origami-based reflectors, a suitable geometry is required, and this represents the main design challenge for such reflectors. To overcome this challenge, a parametric optimization approach is incorporated into the design process. Previous deployable reflector research using the flasher and Miura-Ori pattern showed that parametric optimization is a viable methodology for producing desired designs [15–18], and that such optimization can achieve incremental gains over preceding research using manual analytical design [9, 19].

The concept to be presented in this paper takes the Miura-Ori pattern as a basis for its folding architecture. The Miura-Ori pattern is prominently used in deployable structures [20, 21], and has flown on the Space Flyer Unit [22]. Numerous studies on the Miura-Ori pattern have also been conducted for meta-materials and general deployable structures [23–27]. The folding architecture here includes fully-rigid components, double curvature, finite thickness, supporting trusses, as well as single degree-of-freedom (DOF) deployment, features seldom simultaneously achieved.

For origami, a new method to achieve single-DOF folding of doubly-curved Miura-Ori patterns is presented. Incorporation of the Hoberman linkage retains single-DOF under variations of pattern geometry, i.e. it does not impose stringent constraints on pattern geometry like existing doubly-curved Miura-Ori patterns [25, 26]. This opens up design space within which optimal geometries can be pursued. For optimization, a systematic parametrization process is incorporated with Bayesian optimization to create an explainable and efficient design methodology. This framework produces global optimums for the highly nonlinear and non-convex design problem, achieving compact stowage of the reflector along a collision-free strain-free folding trajectory, whilst fulfilling all simultaneous design requirements. For application, the design with its fully-rigid doubly-curved surface panels and supporting trusses provides a unique option for high-precision deployable reflectors requiring compact stowage and good structural performance. It also provides an

automated design tool for producing optimal designs with minimal human intervention.

In this paper, Section III introduces how the folding architecture is derived from the Miura-Ori pattern, Section IV briefly covers the kinematics model used, Section V details the optimization process used to systematically determine key parameters, and Section VI presents an example result, including optimal parameters, exploration of the design space, a detailed mechanical design and its derivative variants, a prototype model, as well as surface error quantification.

III. Reflector Architecture

The proposed optimization approach aims to reduce uncertainty and subjective decisions within the design process, pursuing systematic and explainable design where possible. A baseline architecture is the starting point of this design process. It must provide sufficient design space for the ensuing optimization, whilst not being too large and thus make global optimization intractable. Also, many reflector characteristics are fixed by the architecture, and can no longer be changed during optimization. Therefore, the choice of architecture is crucial for overall design.

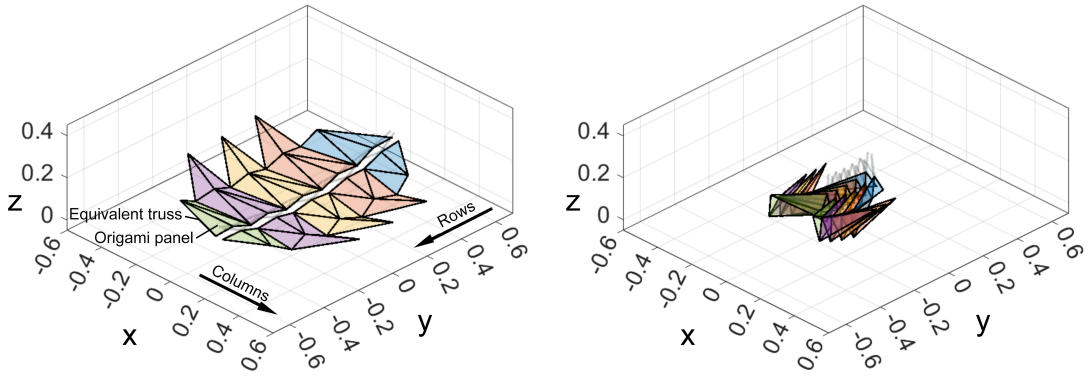
A. Miura-Ori supporting truss

The reflector architecture proposed here starts with a supporting truss based on the Miura-Ori pattern, where structural members and revolute hinges of the truss are kinematically equivalent to panels and creases of the origami pattern. The Miura-Ori pattern is defined here in three-dimensional space instead of a flat plane, in order to conform to the doubly-curved reflector surface. This modification loses the single-DOF rigid foldability of two-dimensional Miura-Ori patterns. To recover foldability for this non-flat pattern, each quadrilateral panel of the original Miura-Ori pattern is split into two triangular panels. Such a modification however introduces multiple degrees of mobility, and further constraints must be added to recover single-DOF folding.

There are several desirable features provided by the Miura-Ori pattern. First, foldability is guaranteed as long as geometric conditions are met, as shown by previous applications [25, 26] and mathematical derivation [28]. The condition for foldability is that all fold angles must remain the same sign throughout deployment, and this is satisfied by having the Miura-Ori pattern be corrugated at full deployment. Second, corrugation of the Miura-Ori pattern has the added effect of giving the reflector structural depth, which is beneficial for its overall stiffness. Third, the modified Miura-Ori pattern consists of 6-crease vertices, which have predictable kinematics behaviors favorable for optimization.

Figure 1 illustrates the basic geometric representation of the supporting structure, where solid black lines represent the creases of the pattern, and enclosed facets are the panels. The truss structure here follows the geometry of creases in the origami pattern. Details including hinge placement etc. are covered in the example mechanical design. Following the grid layout of the Miura-Ori pattern, panels can be organized into rows and columns. Column-wise mirror symmetry is introduced for columns on opposite sides of the symmetry plane (y-z plane). In Figure 1, a 2-column 5-row configuration is shown. Column 1 is adjacent to the symmetry plane, and consists of 5 rows. Column 2 is attached to column 1, and

only consists of 3 rows, two fewer than the previous to maintain kinematics constraints. The folding architecture is extendable to arbitrary numbers of columns and rows, with the only constraint being each column must have at least two fewer rows than the previous. For deployable reflectors, the 2-column 5-row configuration selected here provides good balance between stowage efficiency, structural rigidity, mechanical complexity and surface precision.



(a) Deployed state. **(b) Stowed state.**

Fig. 1 Supporting truss based on the Miura-Ori pattern.

B. Hoberman linkage spine

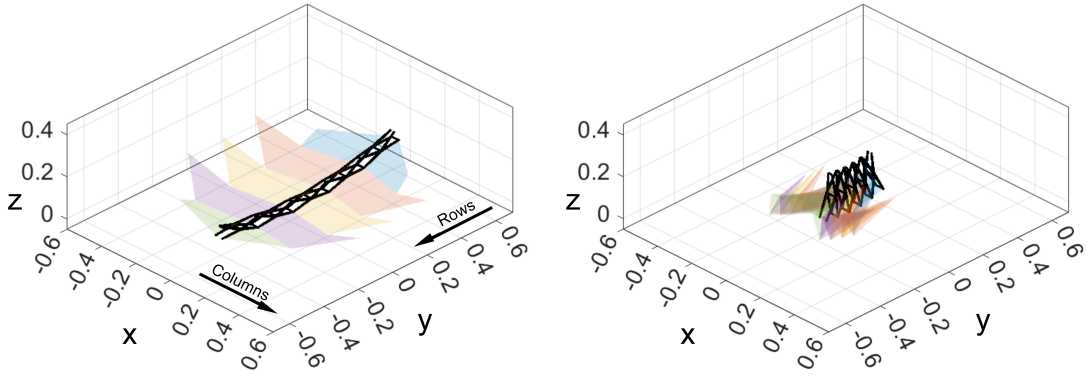
A central spine based on the Hoberman linkage [29, 30] is added to complement the Miura-Ori supporting truss. Its two main functions are restoring single-DOF kinematics, and introducing row-wise periodicity.

To restore the single-DOF kinematics lost by triangulating panels, the degree of kinematic mobility of the pattern must be reduced. Previous research has studied methods to remove triangulation and achieve single-DOF rigid foldability of three-dimensional surfaces with quadrilateral panels [25, 26]. While these are remarkable mathematical findings, in the context of deployable reflectors the stringent geometric constraints mean that folded patterns cannot be freely adjusted for compactness. The Hoberman linkage used here provides an alternative solution. By mounting the Miura-Ori pattern to the central Hoberman spine, additional kinematic constraints are imposed to the root vertices of the pattern. This constraint propagates along each column of the Miura-Ori pattern, ensuring single-DOF folding for arbitrary numbers of columns. Meanwhile, the geometry of the triangulated panels can still be freely adjusted, and provides sufficient design space to find optimally-stowed configurations. This novel kinematic design not only makes the reflector design here possible, but also has potential for applications beyond deployable reflectors.

Introducing row-wise periodicity is necessary for making the global optimization tractable. To define the exact shape of the Miura-Ori pattern, there are numerous dimensions which must be determined. At the most extreme, every vertex of the pattern can be independently placed, corresponding to 3 coordinates each, and this number of unknown variables will be intractable to optimize. Column-wise symmetry halves the number of variables, and row-wise periodicity can further reduce it. By using identical linkages at each row, the Hoberman spine can be made periodic to provide the

necessary boundary conditions for a row-periodic Miura-Ori truss.

As shown in Figure 2, a single actuation on the Hoberman spine will make it contract or expand, thereby controlling single-DOF movement of all trusses on either side of the spine. Each row of the spine is identical, creating a periodic circular arc shape. Every row of trusses can hence also be identical in shape and kinematics to create a curved truss profile. After imposing symmetry and periodicity, the only unique geometry to be modeled and designed is reduced to a single row on one side of the spine. It should be noted that periodicity and symmetry are only introduced to simplify design, and that single-DOF foldability can be achieved without periodicity or symmetry.



(a) Deployed state. **(b) Stowed state.**

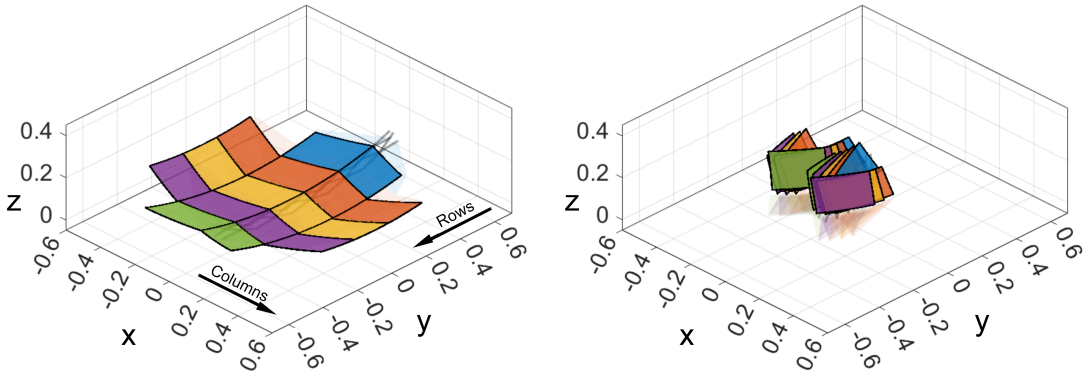
Fig. 2 Reflector spine based on the Hoberman linkage.

C. Surface panels

The reflector surface is segmented into a number of panels, which are rigidly attached to certain members of the supporting truss. Movement of the supporting truss drives movement of the surface panels. In the fully deployed state, the surface panels form the reflector surface, while during stowage they are to move without colliding with one another and stow into a compact shape. Similar mounting of surface panels to trusses has previously been studied for a single column of panels [31, 32]. More recent algorithmic designs of origami structures consider complex folding without attached surface panels [23, 26]. Here, efficient folding of a multi-column multi-row origami truss with attached surface panels is pursued. Collision between various surface panels and supporting structures poses a highly non-convex and nonlinear constraining condition, preventing the synthesis of heuristic or algorithmic approaches and necessitating an optimization approach for obtaining feasible designs.

As shown in Figure 3, the panels are defined in a periodic and symmetric fashion, alongside the supporting truss. Imposing symmetry and periodicity to a doubly curved reflector surface constrains its geometry to a rotated surface parallel to the x-axis. To also have rotational symmetry in the z-axis, a spherical surface is adopted. Other aspherical geometries such as paraboloids or hyperboloids only slightly deviate from a sphere for reflectors of moderate focal lengths. The deviation is usually within the thickness of reflector panels, so aspherical surfaces can still be

accommodated by spherical collision models. On the other hand, spherical reflectors can also be desirable, as its symmetry allows advantages including wide field-of-view and efficient beam steering [33]. Such spherical-surface reflector systems have been tested in flight [34].

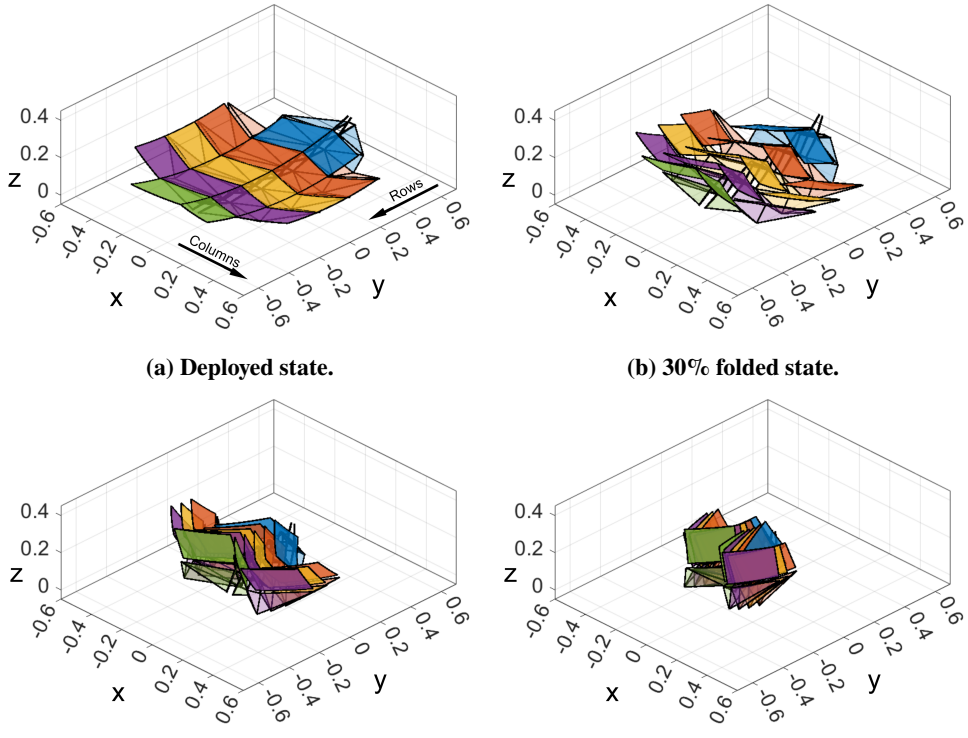


(a) Deployed state. **(b) Stowed state.**

Fig. 3 Reflector surface panels. The underlying truss structure is shown as translucent.

D. Combined reflector architecture

Figure 4 shows the folding sequence of the combined reflector structure, in which some key points can be noted. The stowage process reduces the reflector size in the x and y directions, while increasing its size in the z direction, and overall volume decreases during stowage.



(a) Deployed state. **(b) 30% folded state.**

(c) 80% folded state. **(d) Stowed state.**

Fig. 4 Overall folding sequence of reflector with combined surface panels and supporting truss.

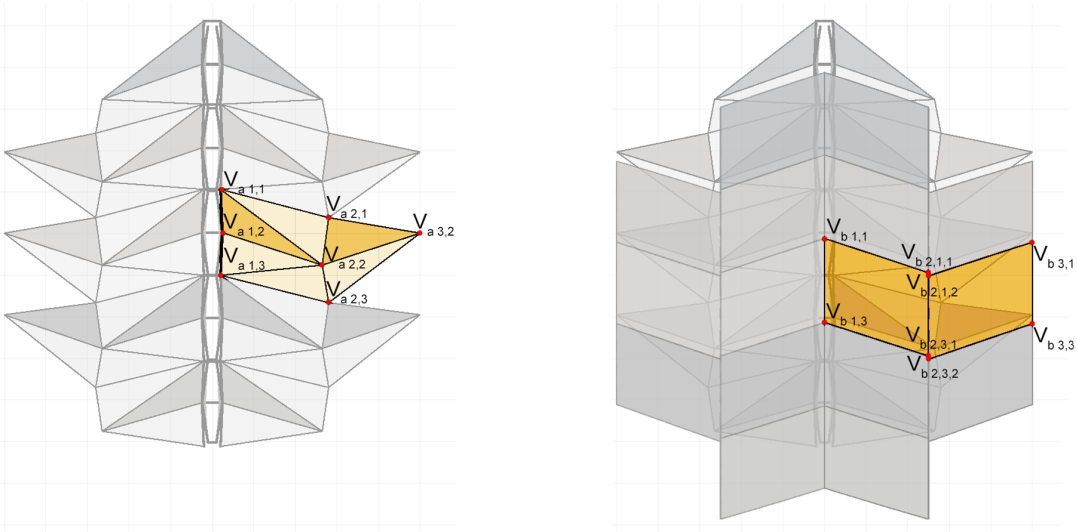
Panel-truss collision is readily eliminated as surface panels remain above the trusses in all states. Panel-spine collision is also eliminated, even though the Hoberman linkage ribs extend above the trusses, due to the folding direction of the column-1 panels. Panel-panel collision can occur between panels of same column, or adjacent column. Collision between same-column panels can be easily eliminated, as panels separate quickly during folding, and nest well due to periodicity. Collision between panels of adjacent columns is the main issue. When full stowage is approached, panels tend to collide at the edge between columns. To avoid this, panels are attached so that columns face outwards and inwards alternately. The top surfaces of all panels in column 1 face outwards and nest compactly for stowage, while all panels in column 2 have their top surfaces facing inwards. Were column 3 to be added, panel top surfaces would face outwards again. This opposite-facing configuration is vital in avoiding collision between adjacent columns, using a configuration similar to an offset split line method [16, 17].

E. Detailed dimensions and overall parameters

With the overall architecture of the reflector structure now specified, a systematic parametric dimensioning of the shape is needed to allow for parametric optimization. Following the typical approach of origami structures, geometries are defined based on vertex coordinates. The supporting truss, spine and surface panels are all rigid bodies which are based on surfaces, lines and finally vertices. A Cartesian dimensioning of vertices is hence used to specify the detailed geometry. Following the periodicity and symmetry introduced previously, the vertices which need to be considered for the supporting structure and surface panels of a 2-column pattern are shown in Figure 5.

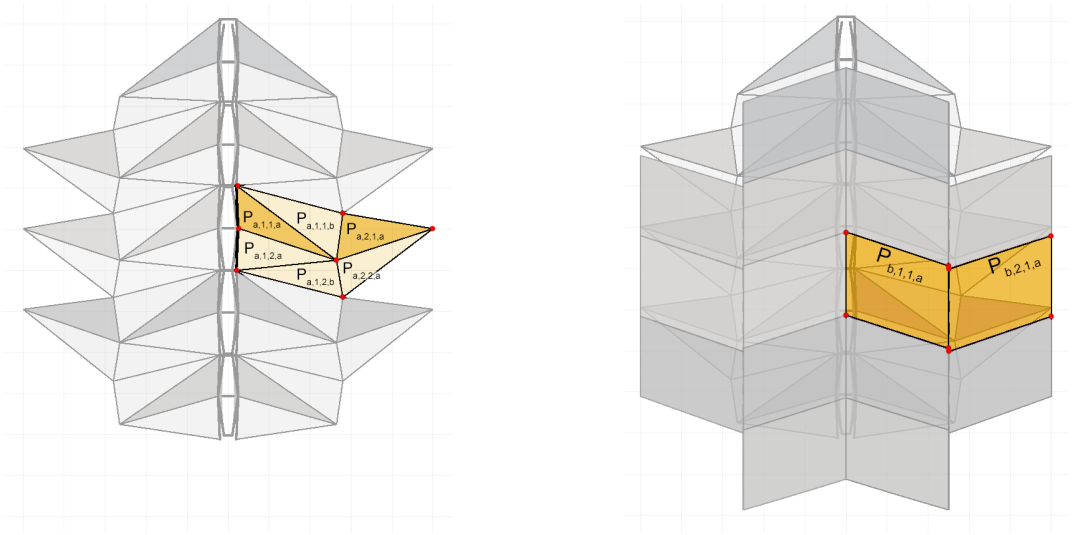
Here vertices $V_{a,i,j}$ denote those on the supporting truss, which is coupled with the Hoberman linkage spine, and $V_{b,i,j}$ denote those on the surface panels. Subscripts i, j denote the x-direction and y-direction index of the vertices. Each V_a vertex has three Cartesian coordinates, while V_b need only be defined on the projected x-y plane. Due to periodicity, additional rows will not lead to additional unique vertices, but each additional column will lead to additional V_a vertices and V_b vertices. Note also how some V_b vertices contain two slightly offset points, as split lines of the surface panels are not made to be always coincident at a vertex. The coordinates of these vertices form the largest set of variables which affect the reflector shape. Section V will detail how the detailed dimensions formed by these vertex coordinates are systematically determined.

For completeness and clarity, Figure 6 shows the labeling of reflector panels. Again due to periodicity and symmetry, only a single row needs to be defined. Supporting panels $P_{a,i,j}$ are denoted by their top-left corner vertex, with $P_{a,i,j,a}$ and $P_{a,i,j,b}$ denoting the inner and outer triangular halves of a quadrilateral Miura-Ori panel. Surface panels share the naming of the supporting panel to which they are attached. Following the opposite-facing panel configuration, for the first two columns, surface panels $P_{b,i,1,a}$ are attached to $P_{a,i,1,a}$. Denoting the crease between $V_{a,i1,j1}$ and $V_{a,i2,j2}$ as $C_{a,(i1,j1)-(i2,j2)}$, $P_{b,1,1,a}$ and $P_{b,2,1,a}$ are cantilevered along $C_{a,(1,2)-(2,2)}$ and $C_{a,(2,2)-(3,2)}$ respectively.



(a) Supporting structure. **(b) Reflector surface.**

Fig. 5 Labeling of vertices.



(a) Supporting structure. **(b) Reflector surface.**

Fig. 6 Labeling of panels.

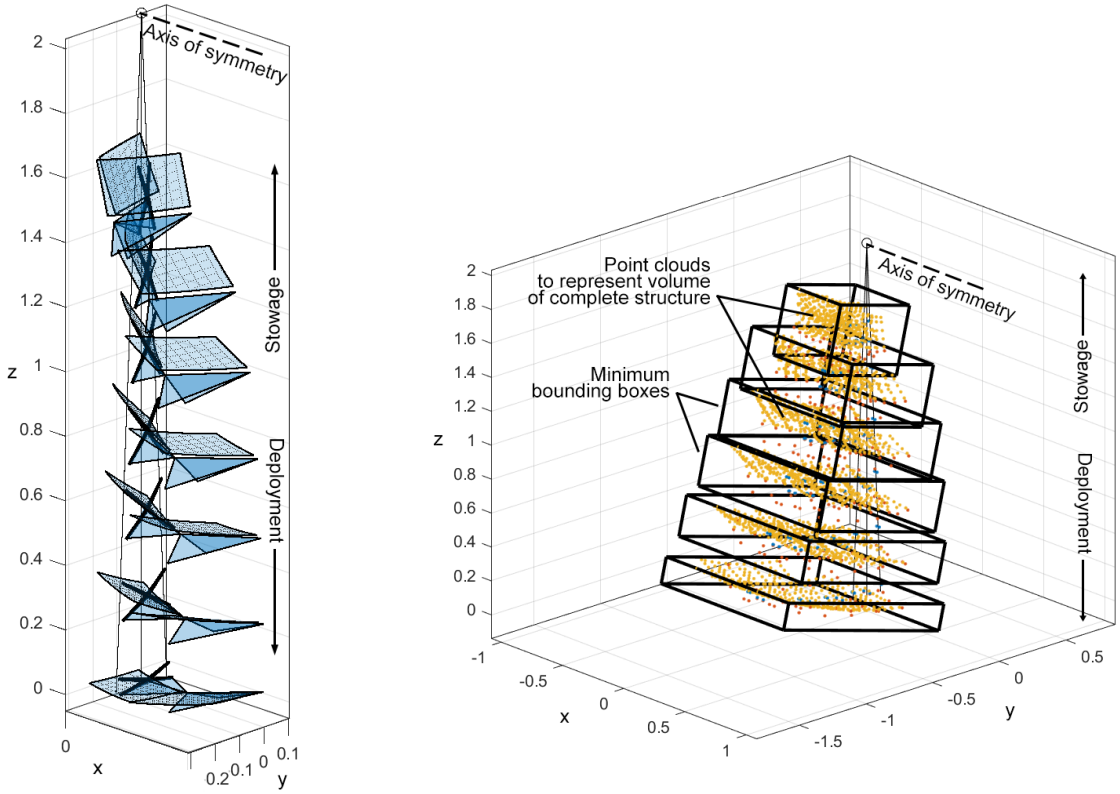
A number of overall design parameters provide partial constraints to the detailed dimensions. Such parameters depend on design requirements for the reflector itself, and thus are fixed during optimization. Table 1 lists some of these overall parameters. The number of rows and columns of the reflector will control the overall aspect ratio of panels, and in turn impact the stowed shape of the reflector, with z-direction size traded against x and y-direction size. Focal length will be determined by the RF or optics design of the reflector, while dimensions like panel thickness and structural depth will be determined by structural considerations. Thicker and more curved components are more difficult to stow. Such overall design parameters convey overall design requirements and bring clear effects onto the reflector geometry.

Table 1 List of some reflector overall design parameters.

Parameter	Definition	Overall Effect
N_r	No. of rows in the reflector	Controls stowed state z-direction height and y-direction length
N_c	No. of columns in the reflector	Controls stowed state z-direction height and x-direction width
f	Reflector focal length	Affects reflector curvature and stowed state compactness
t_p	Reflector panel thickness	Affects mountain-fold vertex placement and stowed state compactness
d_d	Reflector structural depth	Affects valley-fold vertex placement and stowed state compactness

IV. Reflector Folding Kinematics Model

To carry out optimization, a kinematics model is needed to rapidly and robustly perform evaluation of objective functions for various geometries. This is briefly introduced. Similar to methods adopted previously [15, 17], the folding kinematics of the reflector is modeled by considering all components as rigid bodies, adding kinematic constraints that relevant vertices be coincident, applying a single actuation to control the overall folding, and solving for each component's position and orientation in space. Due to periodicity and symmetry, only a single row of the reflector needs to be modeled to capture all unique kinematics. Rotations and mirroring can then be applied to derive descriptions of the complete geometry. The core kinematics model of a single row is illustrated in Figure 7a. To allow convenient rotation, the axis of rotational symmetry is fixed in space, and the Hoberman linkages expand and contract around the axis, subsequently driving movement of panels. As annotated in Figures 7a and 7b, the axis of symmetry passes through the center of the sphere formed by the reflector surface as well as the Hoberman linkage, and is parallel to the x-axis. Collision between panels are evaluated by calculating the distance between point clouds representing the finite-thickness structure, using periodicity when necessary. Web-shaped grids of points are generated as the most computation-saving point cloud for collision modeling. This is formed by generating a square grid of points, and removing sections of the grid. As shown in Figure 7a, the result is lines of points with small within-line interval, arranged in rows and columns with large inter-line interval. This captures the surface shape to satisfactory fidelity with minimal use of points. Using these points, parallelized distance evaluation is carried out. A point cloud is also adopted to evaluate overall reflector size. A sparser set of points is generated to capture the shape of supporting trusses, the Hoberman linkage spine, and surface panels. Rotation and mirroring are used here to obtain the full reflector geometry. Along each step in the folding trajectory, a minimum bounding box [35] is found around the reflector. These point clouds and minimum bounding boxes are illustrated in Figure 7b. Dimensions of the bounding box provide necessary size information for evaluation of the objective function. Other information needed during optimization are also extracted from this model.



(a) Single row resolved in kinematic model. **(b) Complete reflector geometry resolved in collision model.**

Fig. 7 Folding sequence calculated by the kinematics and collision models, showing reflector panels and trusses which are resolved in each model.

V. Reflector Geometry Optimization

Section III detailed how the overall folding architecture is designed and dimensioned. This section will proceed to explain how every dimension of the architecture is determined to create an optimal folding design. The same 2-column 5-row architecture is used as an example, and this methodology is repeatable for any number of columns or rows.

A. Reduction of unknown variables

Starting from the vertices shown in Figure 5, all surface and supporting structure coordinates are summarized in Tables 2 and 3. Viewing each coordinate as an unknown variable, some can be determined by design considerations, while the remainder are passed to optimization. Here, variables which cannot be determined are marked in bold as unknown, and those which can be determined have the justification listed. The following discussion will detail how variables are determined.

Starting with the surface panels, the approach adopted here is to fully prescribe the V_b coordinates and only pass V_a coordinates to optimization. This allows more design control over the surface panel geometry. Due to periodicity, all $V_{b,i,3}$ coordinates are rotations of $V_{b,i,1}$, and are thus dependent. The x and y coordinates for $V_{b,i,1}$ are distributed evenly so that the reflector has unit width and length. For the 2-column reflector here, this means that $X_{b,1,1} = 0$, $X_{b,2,1} = 0.25$

and $X_{b,3,1} = 0.5$. The coordinate $Y_{b,1,1}$ is also calculated so that the total projected y-direction length of the reflector is equal to 1. Finally, $Y_{b,2,1}$ and $Y_{b,3,1}$ are dependent on the supporting truss geometry. A y-offset approximately equal to panel thickness is prescribed between $V_{b,i,1}$ and $V_{a,i,2}$, so that panels sit above trusses when stowed. Tests show that small changes to Y_b do not affect collision, and thus do not significantly affect stowage.

The supporting trusses have more complex geometry. Some coordinates are prescribed and others are left to be optimized. Similar to the surface panels, periodicity means that vertices $V_{a,i,3}$ are rotations of vertices $V_{a,i,1}$, making their coordinates completely dependent. Starting with $V_{a,1,1}$, its coordinates can be completely prescribed, with $X_{a,1,1}$ determined by the designed width of Hoberman linkages, and $Y_{a,1,1}$ and $Z_{a,1,1}$ determined by the Hoberman linkage cross-section. The Hoberman linkage has a prescribed depth, and is made to conform just under the reflector surface. The two tips of the Hoberman linkage spine are placed at $y = 0$ and $y = 1$ respectively, and the sector angle of the Hoberman linkage, i.e. the angle that each repeating section occupies, is calculated according to the design parameters of reflector curvature and number of rows. Similar to $V_{a,1,1}$, $V_{a,1,2}$ is also mostly dependent on the Hoberman linkage geometry. However, $X_{a,1,2}$ is allowed to shift rightwards, in order to adjust the alignment of panels in the y-z plane projection. This alignment is illustrated in Figure 8. Here, each surface panel is of quadrilateral shape, with straight bottom and top edges, and slanted sides. The bottom edges of panels are creases $C_{b,(i,1)-(i+1,1)}$, with geometry driven by creases $C_{a,(i,2)-(i+1,2)}$ on the supporting truss. It is desired to have these creases aligned during stowage, where in the y-z plane projection, they are approximately tangent to the arc formed by the Hoberman linkage. This ensures a compact shape, and as detailed shortly, can be described using the averaged z-component of the direction vectors of creases. Moving onto $V_{a,2,1}$, it is on a valley fold in the pattern, so its z coordinate is placed at a prescribed depth below the reflector surface. The x and y coordinates of $V_{a,2,1}$ are kept floating for optimization. A similar configuration is used for $V_{a,2,2}$. As it is a mountain fold, its z coordinate placed just below the reflector surface. Finally, for $V_{a,3,2}$, $X_{a,3,2}$ is prescribed at the reflector edge, which is $X = 0.5$. Alignment requirements for panels constrain $Y_{a,3,2}$, and $Z_{a,3,2}$ is again placed just below the reflector surface.

Table 2 List of dimensions for surface panels.

$\boldsymbol{V_{b,1,1}}$:	$\boldsymbol{V_{b,2,1}}$:	$\boldsymbol{V_{b,3,1}}$:
X: fixed at symmetry plane	X: prescribed position	X: fixed at reflector edge
Y: prescribed position	Y: prescribed offset	Y: prescribed offset
$\boldsymbol{V_{b,1,3}}$:	$\boldsymbol{V_{b,2,3}}$:	$\boldsymbol{V_{b,3,3}}$:
X,Y periodic	X,Y periodic	X,Y periodic

Table 3 List of dimensions for the supporting structures.

$\boldsymbol{V_{a,1,1}}$:	$\boldsymbol{V_{a,2,1}}$:	
X: prescribed position	**X: Unknown**	-
Y: fixed by Hoberman	**Y: Unknown**	
Z: fixed by Hoberman	Z: fixed valley offset	
$\boldsymbol{V_{a,1,2}}$:	$\boldsymbol{V_{a,2,2}}$:	$\boldsymbol{V_{a,3,2}}$:
X: Unknown	**X: Unknown**	X: fixed at reflector edge
Y: fixed by Hoberman	**Y: Unknown**	Y: constrained by alignment
Z: fixed by Hoberman	Z: fixed mountain offset	Z: fixed mountain offset
$\boldsymbol{V_{a,1,3}}$:	$\boldsymbol{V_{a,2,3}}$:	-
X,Y,Z periodic	X,Y,Z periodic	

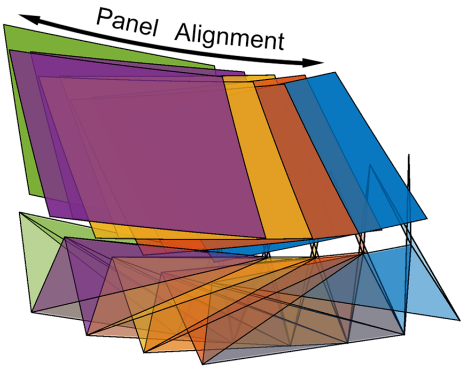


Fig. 8 Alignment of panels on y-z plane.

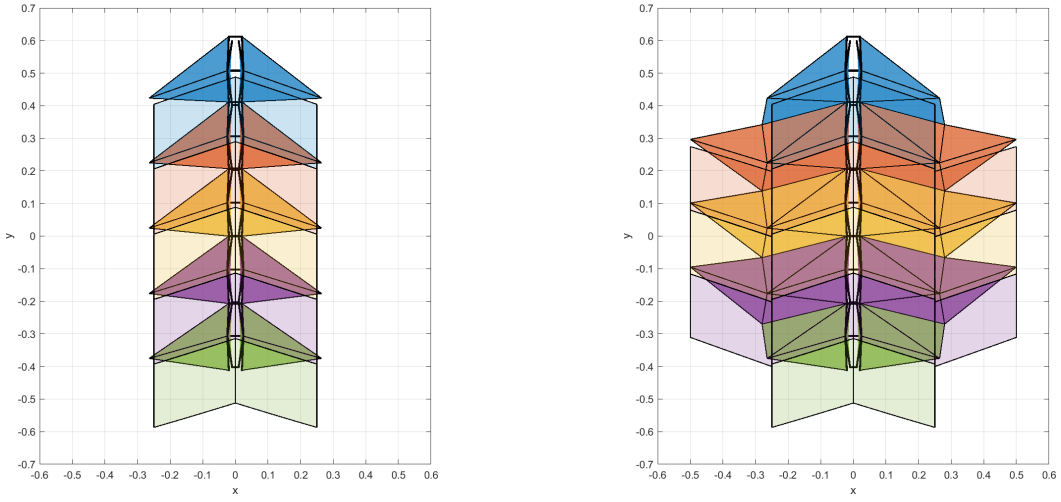
After having prescribed as many coordinates as possible, the remaining unknown variables are $X_{a,1,2}$, $X_{a,2,1}$, $Y_{a,2,1}$, $X_{a,2,2}$ and $Y_{a,2,2}$. These variables cannot be directly prescribed by design considerations, but influence the reflector geometry and folding kinematics, and thus must be optimized to establish a collision-free trajectory to compact stowage.

B. Separation of unknown variables

For the 2-column pattern here, the remaining 5 unknown coordinates include 2 for the first column and 3 for the second column. While it is possible to pass all variables simultaneously into optimization, this would mean a large five-dimensional design space, and exploring the space for robustly finding global optimum becomes difficult. The unique kinematic characteristics of the Miura-Ori truss proposed here are invoked to separate the optimization variables

into smaller groups of 2 and 3 dimensions, exponentially reducing the design space and greatly improving optimization efficiency and robustness.

In the supporting truss, kinematics constraints propagate outwards from the spine across each column of panels. All inner columns of panels can achieve single-DOF motion, independent from any column on the outside. Therefore, optimization can also propagate from the spine, and be conducted sequentially for each column of panels. As illustrated in Figure 9, the first column group consists of the Hoberman spine, along with supporting panels $P_{a,1,1,a}$ $P_{a,1,2,a}$ and surface panel $P_{b,1,1,a}$. For the second column group, supporting panels $P_{a,1,1,b}$, $P_{a,1,2,b}$, $P_{a,2,1,a}$ and $P_{a,2,2,a}$ are added, along with surface panel $P_{b,2,1,a}$. During optimization, the first column is modeled and optimized first, and its geometry is fixed. Afterwards, the second column is added to the model, optimized, and its geometry fixed as well. A third row, and in fact any number of rows, can be added, modeled and optimized in this sequential fashion.



(a) First column group. **(b) Second column group (with first group as base).**

Fig. 9 Layers of the reflector structure: each layer is single-DOF.

C. Optimization of unknown variables

The primary objective for optimization here is to minimize the stowed size of the reflector. To capture this, stowage ratios are used to formulate objective functions. For patterns such as the flasher pattern, the diameter is the key defining metric for stowage [17], while here, the Miura-ori pattern contracts in the x and y directions. Thus, based on bounding boxes previously retrieved in the kinematics model, stowage ratios in the x and y directions are obtained and used.

For the first column, the unknown variables associated with its geometry include $X_{a,1,2}$ and $Y_{a,2,2}$, two variables in total. Stowed size here is driven by both x and y dimensions, so the objective function used for the first column is

$$F_{(X_{a,1,2},Y_{a,2,2})} = \max\left(\frac{D_{X,stowed}}{D_{X,deployed}}, \frac{D_{Y,stowed}}{D_{Y,deployed}}\right) \tag{1}$$

where D_X and D_Y are the lengths of the bounding box of the reflector in the x and y direction. A Bayesian optimization

scheme is used to minimize F with upper and lower bounds placed on each variable. Some additional constraints include checks that fold angles have the correct sign to give the corrugated shape at full deployment, and that self-intersection of the pattern does not occur. The final constraint for the first column is panel alignment, as illustrated by Figure 8. For the first column, shape definition starts from the fully deployed state, and the folding trajectory is calculated until either collision between any two panels is detected, or any fold angle exceeds 180°. This procedure is implemented using the kinematics model introduced in section IV, using bisection methods to minimize expensive collision calculations.

The effect of each optimization variable can be analyzed. First, $Y_{a,2,2}$ controls how skewed the Miura-Ori pattern is. A more skewed pattern will produce a pattern which is elongated in the y direction, while more compact in x, and vice versa. The objective function is designed to find the correct skew where x and y compactness are balanced. Second, altering $X_{a,1,2}$ manipulates the orientation of stowed panels, allowing panels to satisfy the alignment constraint.

Here, the degree of actuation is not fixed, and folding instead stops at where first collision occurs. For each variation in geometry, there is a corresponding maximum possible degree of actuation which is also the most stowed state. This is captured by the modeling and optimization process, and does not need separate design consideration. Essentially, collision constraints are implicitly satisfied during objective function evaluation. In all, the first column optimization problem can be summarized as

$$
\begin{aligned}
\min_{X_{a,1,2},\, Y_{a,2,2}} \quad & F = \max\left(\frac{D_{X,stowed}}{D_{X,deployed}}, \frac{D_{Y,stowed}}{D_{Y,deployed}}\right) \\
\text{s.t.} \quad & X_{a,1,2} \in [X_{min}, X_{max}], \\
& Y_{a,2,2} \in [Y_{min}, Y_{max}], \\
& \forall a \in a_{mountain} : a > 0, \\
& \forall a \in a_{valley} : a < 0, \\
& \frac{1}{N_r}\sum_{n=1}^{N_r}(S_n) \approx 0
\end{aligned}
$$

where a is the fold angle of creases in the deployed state, including mountain and valley creases, and S is the slant of surface panels, quantified by $Z_{a,2,2} - Z_{a,1,2}$ of each row of panels in the stowed state, which is the z-component of each crease $C_{a,(i,2)-(i+1,2)}$. The mean slant, i.e. averaged z-component, calculated over all rows N_r is constrained to approximately zero, in order to obtain alignment of panels.

For the second column, and each following column, optimization takes another procedure, different from the first. Each column has three optimization variables, $X_{a,2,1}$, $Y_{a,2,1}$, $X_{a,2,2}$ in the case of the second column. Observation of the kinematics showed that $0 < X_{a,2,2} < X_{a,2,1}$ is required, therefore in optimization, $0 < rX_{a,2,2} < 1$ is considered instead of $X_{a,2,2}$. The variable $rX_{a,2,2}$ is the ratio between $X_{a,2,2}$ and $X_{a,2,1}$ offsets from $X_{b,2,1}$, defined by $X_{a,2,2} - X_{b,2,1} = rX_{a,2,2}(X_{a,2,1} - X_{b,2,1})$. This mapping ensures the observed kinematic requirements are fulfilled, producing a design space with larger feasible regions and further improving optimization efficiency and robustness.

The geometry of the Hoberman linkage spine and the first column are now fixed and the second column must be optimized without affecting previous results. To do so, the maximum actuation for reflector folding is fixed at the value used by the first column, and the second column is actuated to this extent, regardless of collision and fold angle constraints. To obtain results which are collision-free, an explicit term describing collision is added into the objective function and minimized. Hence, the objective function is set as

$$F_{(X_{a,2,1},Y_{a,2,1},rX_{a,2,2})} = \frac{D_{X,stowed}}{D_{X,deployed}} + \log(n_{col} + 1) \tag{2}$$

where n_{col} is the number of collided points detected between point clouds as introduced in section IV. The explicit collision penalization term $\log(n_{col} + 1)$ allows the objective function to capture collision behavior as a well-behaved function. Meanwhile for the stowage term, only $\frac{D_{X,stowed}}{D_{X,deployed}}$ is considered, and $\frac{D_{Y,stowed}}{D_{Y,deployed}}$ is omitted because only the first column has longest y-length. Minimizing just the x-direction width is sufficient for optimization. The collision term is far larger than 1 when non-negligible collision occurs and returns to zero when collision disappears, while the stowage term takes the range $[0, 1]$. Therefore, the overall objective function is dominated by collision when it exists, and dominated by x-direction compactness within collision-free regions. This allows the optimizer to first search for regions of zero collision, then seamlessly transition to searching for optimal stowage.

Regarding the effect of variables, $Y_{a,2,1}$ controls the skew of the Miura-Ori pattern, and significantly impacts the folding kinematics. The two x coordinates $X_{a,2,1}$ and $X_{a,2,2}$ have combined effects on reflector folding. When the two move together, it effectively changes the offset between the hinge location of crease $C_{a,(2,1)-(2,2)}$ and that of the split line between surface panels $P_{b,1,1,a}$ and $P_{b,2,1,a}$, affecting the adjacent-column collision between these panels. When $X_{a,2,1}$ and $X_{a,2,2}$ move separately, the offset between them affects the rotation of $P_{b,2,1,a}$, also affecting collision.

Apart from the optimization variables, some other coordinates are prescribed here. To fulfill alignment requirements, $Y_{a,3,2}$ is solved so $\frac{1}{N_r}\sum_{n=1}^{N_r}(S_n) \approx 0$ for the second column. In addition, the coordinates of $V_{a,2,2}$ are derived by extrapolating according to the value of $rX_{a,2,2}$, along the direction vector of crease $C_{a,(1,2)-(2,2)}$ carried over from optimization of column 1. This is done so that the hinge placement and orientation of $C_{a,(1,2)-(2,2)}$ are preserved and the kinematics of the first column are not affected by optimization the second column.

In essence, two translation DOFs of the second column are pinned by existing geometry, x-direction translation is controlled by tandem movement of $X_{a,2,1}$ and $rX_{a,2,2}$, and the three rotational DOFs are controlled by $Y_{a,2,1}$, opposite movement of $X_{a,2,1}$ and $rX_{a,2,2}$, and the derived variable $Y_{a,3,2}$. The optimization problem of column 2 is

$$
\begin{aligned}
\min_{X_{a,2,1},\, Y_{a,2,1},\, rX_{a,2,2}} \quad & F = \frac{D_{X,stowed}}{D_{X,deployed}} + \log(n_{col}+1) \\
\text{s.t.} \quad & X_{a,2,1} \in [X_{min}, X_{max}], \\
& Y_{a,2,1} \in [Y_{min}, Y_{max}], \\
& rX_{a,2,2} \in [0,1], \\
& \forall a \in a_{mountain} : a > 0, \\
& \forall a \in a_{valley} : a < 0, \\
& \frac{1}{N_r} \sum_{n=1}^{N_r} (S_n) \approx 0
\end{aligned}
$$

where the constraints are carried through. Layers 3 and beyond can be optimized in a process similar to layer 2. This section has briefly introduced how the sequential optimization procedure is carried out. Using this methodology, optimal geometric parameters can be systematically obtained. Bayesian optimization is used for minimization of the objective function, as it is compatible for nonlinear non-convex objective functions, and requires fewer evaluations of the objective function. The design process commences with definition of parameters such as reflector curvature and depth etc. Sequential optimization of unknown geometric parameters is then completed using Bayesian optimization, outputting optimal geometries. All calculations are implemented in MATLAB [36].

VI. Optimization Results

To demonstrate the validity of the proposed architecture and design methodology, an example reflector is designed. The 2-column 5-row configuration is again selected. The side lengths of the reflector, i.e. reflector width and length in the x and y directions are set as equal, and used for normalization. Focal length is selected at 100% of side length, panel thickness and truss diameter are set at 1% of side length, and structural depth is set at 4.5%.

A. Optimal geometric parameters

Table 4 lists the optimal geometric parameters produced through Bayesian optimization. These parameters complete the full set of design variables required for definition of the overall reflector shape. Optimization is first carried out for the first column group, to determine $X_{a,1,2}$ and $Y_{a,2,2}$. Subsequently, optimization of the second layer determines $X_{a,2,1}$, $Y_{a,2,1}$ and $rX_{a,2,2}$. Figures 10 and 11 show the evolution of objective function evaluation for the first and second columns respectively. The horizontal axis is iteration number, while the vertical axis is objective function value. Blue points indicate evaluations where all constraints are satisfied, while red crosses indicate evaluations where some constraints are not satisfied. The black and green lines indicate estimated and observed minimum objective function respectively. The

first column involves two optimization variables, and complex collision does not occur, so 120 evaluations is adequate for robustly recovering global optimum. Repeated tests show the optimal objective function value and corresponding optimization variable values can all be recovered with a repeatability within 5%. In contrast, the second column involves three optimization variables, and complex adjacent column collision increases nonlinearity within the design space. As a result, 800 evaluations were needed to robustly recover optimum points with good accuracy. In Figure 11, effects of the compound objective function including both collision and stowage ratio terms can be observed. Points where significant collisions occur have objective function larger than 1, and are only occasionally explored. Most evaluation points are focused on accumulating information in collision-free zones below 1, which are clearly differentiated.

Table 4 Optimal geometric parameters.

First column		Second column		
$X_{a,1,2}$	$Y_{a,2,2}$	$X_{a,2,1}$	$Y_{a,2,1}$	$rX_{a,2,2}$
0.0246	-0.0759	0.2800	0.0364	0.48614

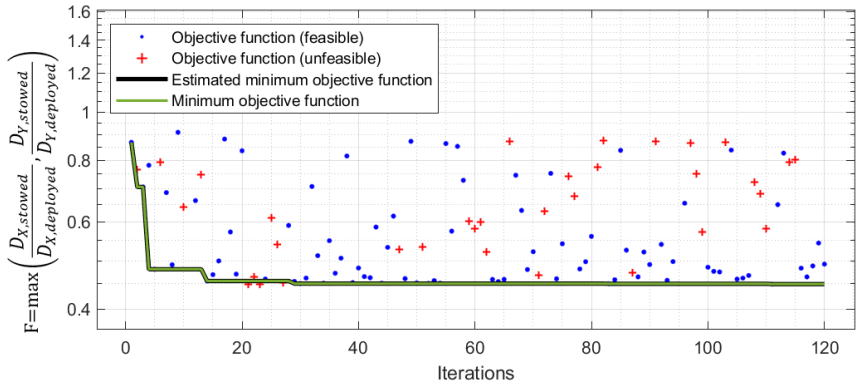


Fig. 10 Evolution of objective function for first layer optimization.

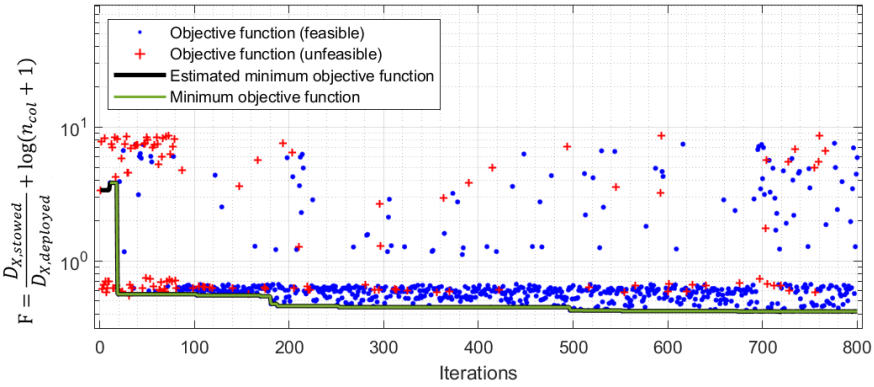
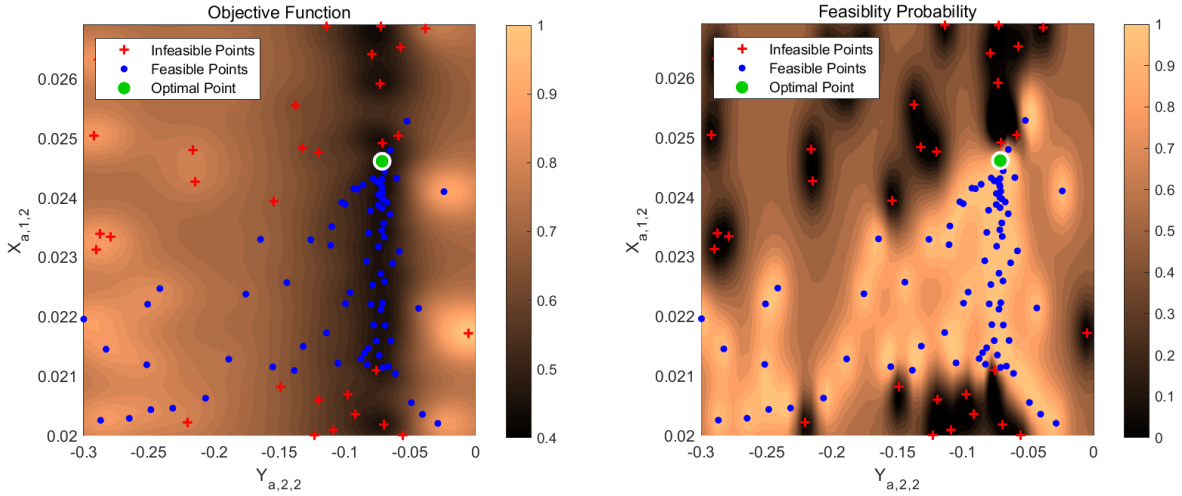


Fig. 11 Evolution of objective function for second layer optimization.

B. Design space exploration

The optimal geometric parameters correspond to a single point in the design spaces of the first and second column, which are two-dimensional and three-dimensional respectively. Information on the topology of this space is usually not pursued during design. Here, however, the use of Bayesian optimization means data points are collected throughout this space, at points incrementally selected from the posterior objective function modeled from preceding points. With this data being available, there is the luxury of fitting a surrogate model to examine the behavior of various metrics throughout the design space. To do so, Gaussian process regression models are fitted to available data sets obtained from optimization. The ARD Matérn 5/2 kernel [37, 38] is used, with variance assumed to be small because the kinematics model is deterministic and each evaluation point is uncertainty-free. This corresponds to the model used during Bayesian optimization. While it is prohibitively slow to evaluate the entire design space using exact models of the reflector, fitted models can be rapidly evaluated across the design space. Here the objective function and feasibility probability for both the first and the second columns are examined. The objective function is $\max\left(\frac{D_{X,stowed}}{D_{X,deployed}}, \frac{D_{Y,stowed}}{D_{Y,deployed}}\right)$ for the first column, and $\frac{D_{X,stowed}}{D_{X,deployed}} + \log\left(n_{col}+1\right)$ for the second column. Feasibility probability describes whether all constraints have been satisfied, taking a value of 1 when all constraints are met, and 0 when otherwise.

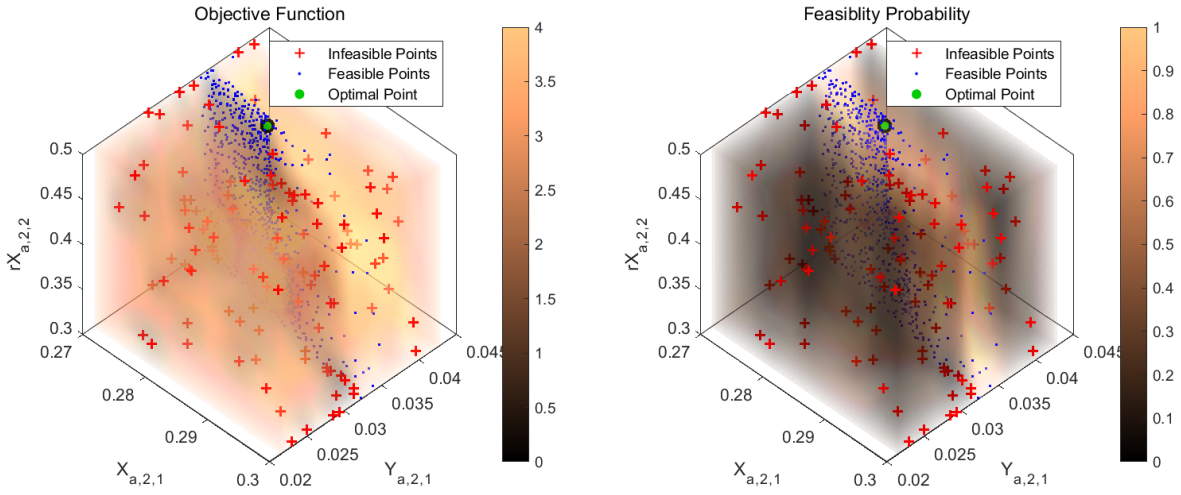


(a) Objective function. **(b) Feasibility probability.**

Fig. 12 Fitted functions for optimization of the first column.

Figure 12 shows the results from optimization of the first column, plotted as contours over the two variables $X_{a,1,2}$ and $Y_{a,2,2}$. The optimal point used for the example design here is indicated in green. Coherent with Figures 10 and 11, the blue dots represent points where the kinematics model was used for evaluation of the objective function, and constraints are met, while the red crosses indicate those where some constraints were not met. Here, it can be seen how the objective function is convex along $Y_{a,2,2}$, and less so along $X_{a,1,2}$. The variable $Y_{a,2,2}$ controls how skewed the Miura-Ori panels are, which by typical Miura-Ori behavior, controls whether the folded shape is more elongated

in the x or y direction. Due to the objective function formulation, minimum occurs when x and y direction stowage ratios are equal, thus convexity appears. Upper and lower bounds on $X_{a,1,2}$ can be seen, where the mean panel slant $\frac{1}{N_r}\sum_{n=1}^{N_r}(S_n)$ exceeds defined tolerances, and the alignment constraint illustrated in Figure 8 is no longer satisfied. A feasible region can be clearly observed in Figure 12b. Irregularities in the fitted objective function arise, partly from artifacts in Gaussian process regression, and partly due to collision between irregular geometries of the surface panels.



(a) Objective function. **(b) Feasibility probability.**

Fig. 13 Fitted functions for optimization of the first column.

Figure 13 shows the results from optimization of the second column, plotted in three dimensions over the three variables $X_{a,2,1}$, $Y_{a,2,1}$ and $rX_{a,2,2}$. A narrow feasible region along $Y_{a,2,1}$ can be observed, while an upper bound and some lower bound can also be observed for $X_{a,2,1}$ and $rX_{a,2,2}$. Any incorrect $Y_{a,2,1}$ values produce infeasible results, while results are less sensitive to the small movements of $X_{a,2,1}$ and $rX_{a,2,2}$. The cause for such responses is local collision between panels of columns 1 and 2, at their corners. This is illustrated in Figure 16a. With any deviation from optimal, collision occurs, and restricts folding, leading to higher objective function values, or infeasible results. The complex and irregular 3-D design space here is what requires Bayesian optimization.

Such exploration of the design space gives additional confirmation that the global optimum has been reached by the design process. This is a useful surrogate when analytical methods cannot be used to provide understanding of the design. This analysis also illustrates the advantage of using Bayesian optimization. The nonlinear non-convex design space, especially that of the second column, makes it challenging to reliably use gradient-based methods. Also, such methods cannot ensure global optimum is reached. In contrast, Bayesian optimization is suitable for a number of reasons. First, the number of optimization variables is low, within the capabilities of Bayesian methods. Second, the nonlinear non-convex design space topology does not inhibit performance of the gradient-free optimizer. Third, the Bayesian method requires minimal tuning of the optimizer, lending itself well to an automated design tool.

C. Example mechanical design

Using the optimal geometric parameters from numerical results, the underlying kinematics of the reflector is defined. A detailed mechanical design can then be made based on such kinematics. Figures 14 and 15 show the resulting detailed design which fully resolves surface panels, supporting trusses, the Hoberman linkage, as well as various hinges.

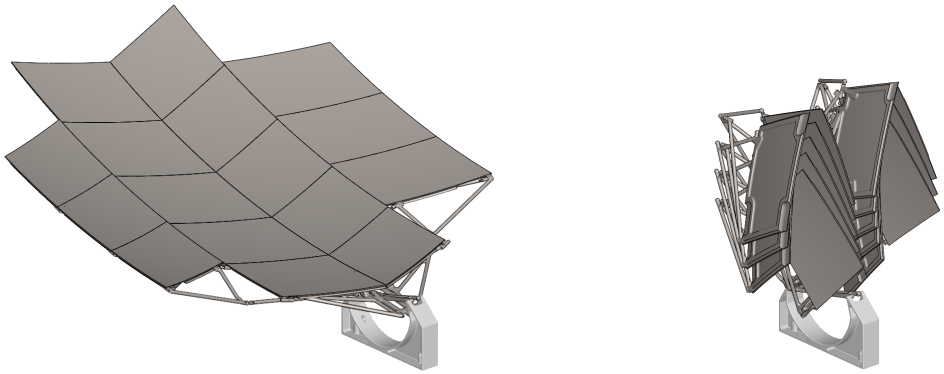


Fig. 14 Isometric view of deployed and stowed reflector.

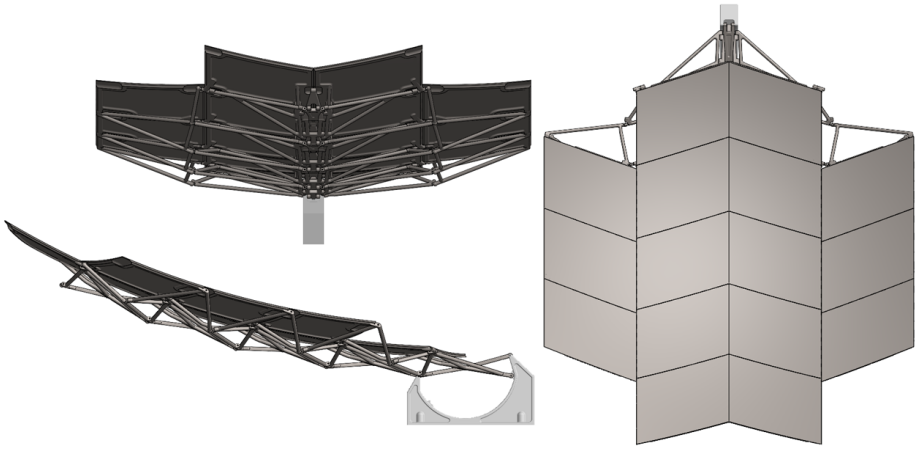
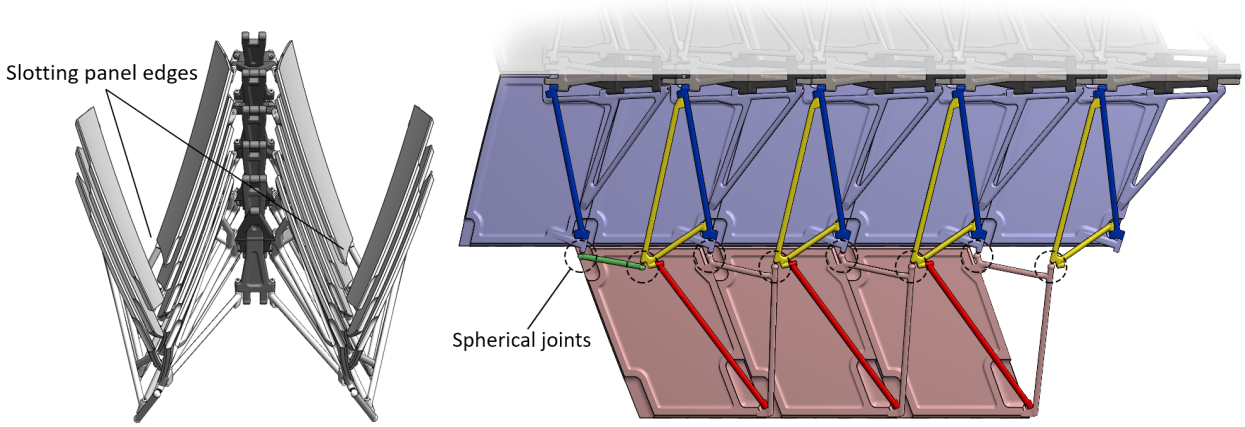


Fig. 15 Deployed reflector orthogonal views.

In the deployed state, the reflector has a double curvature, with the surface panels forming a segmented spherical surface. The closest fitting paraboloid to this surface has the specified focal length of 100% side length. The trusses are corrugated, forming a stiffening support behind the surface panels with a uniform structural depth. In the stowed state, the panels of each column stow together compactly, but there is no collision between any panel or supporting structure, throughout the entire trajectory from the fully deployed to the fully stowed state. As shown in Figure 16a, at the border between columns, panels on one side slot into the vacancies between panels on the other side. This is a highly optimal geometry enabling compact stowage, which would be difficult to achieve through manual trial-and-error. This particular feature shows the value of the optimization approach, and it is also notable how the mathematical construction here can

yield a feature which humans can comprehend as a good design. Alignment of the panels is also satisfied, as mandated by constraints during optimization. The bounding box of the stowed reflector has approximately 41.8% x-width, 44.3% y-length 262% z-height and 51.2% volume, compared to that of the deployed state. This result shows that the proposed Miura-Ori architecture is valid, and the proposed methodology can yield optimal designs.

Some detailed designs are added to the baseline geometry obtained from optimization. Whilst preserving the kinematics, changes are made to accommodate hinges, and to simplify the structure. Panel $P_{a,1,1,b}$ is eliminated except for the last row, where it is simplified to a single bar member. All other panels are also simplified to partial trusses which provide just enough structural support and kinematic constraint. Hinges are added as small revolute joints at correct angles near truss intersections. The resulting trusses can be observed in Figure 16b. The same figure also shows how vertices $V_{a,2,1}$ and $V_{a,2,2}$ are designed as spherical joints. Using the spherical joints allows a direct load path between $P_{a,1,1,a}$ and $P_{a,2,1,a}$. With the baseline origami geometry, this load path would have passed through multiple panels and needed multiple revolute hinges. The spherical joints therefore simplify both the mechanical design and the load path, increasing stiffness and reducing mass.



(a) Compactly slotted panel edges. **(b) Simplified trusses and spherical joints.**

Fig. 16 Notable features of detailed mechanical design.

D. Derivative variants

Due to the periodicity of the reflector geometry and column-wise propagating kinematics of the Miura-Ori truss, derivative variants can be obtained from an existing design without needing any additional design work. Using periodicity, rows of panels can be added and subtracted arbitrarily, under the guarantee that collision-free compact stowage is still viable. This allows post-optimization adjustment of reflector y-direction length, along with changes in focal ratio. More rows will lead to a longer reflector in y, and a lower focal ratio reflector, i.e. a deeper shape. It will also mean a more lengthy load path which passes though more joints, so the number of rows is limited in practice, though the geometry is valid even for a full ring of Hoberman linkages and panels. Using propagating kinematics, columns can

also be added and subtracted arbitrarily, whilst retaining single-DOF kinematics at each column, as long as optimization results have been obtained. This allows post-optimization adjustment of x-direction length, again changing focal ratio. Newly-added columns need to have their geometry optimized, which is simple thanks to separation of variables. As column number increases, panels become less compactly stowed, due to spacing between adjacent columns, and the load path is also lengthened, converging from tip columns to the Hoberman linkage before passing to the reflector base, thus the practical number of columns is also limited. Figure 17 shows two examples of possible derivative variants, with added rows and subtracted columns respectively. For practical applications, the 2-column 5-row configuration originally considered is near the upper limit of rows and columns, with single-column configurations being equally desirable. The 2-column and 1-column configurations are both considered in prototyping.

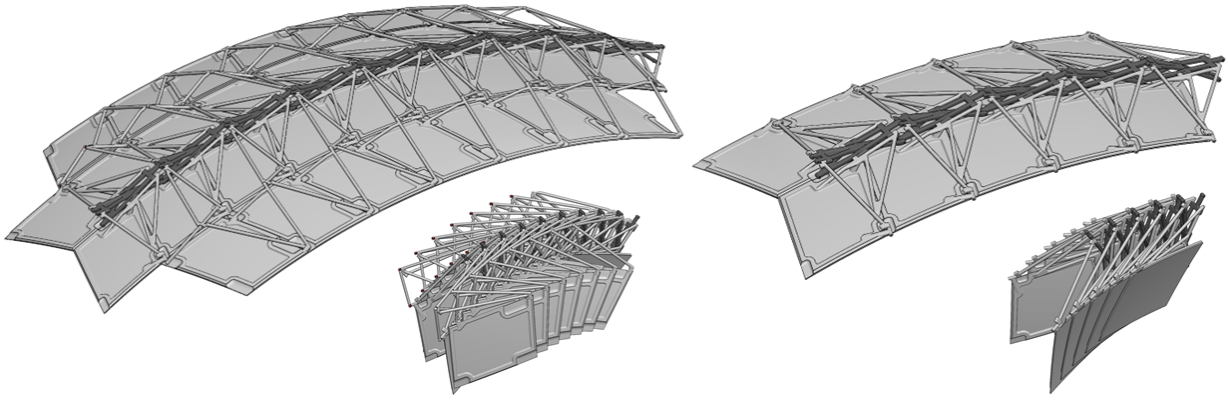


Fig. 17 Example derivative reflector variants.

E. Prototype model

In order to validate mechanical design, a prototype model is manufactured. The main reflector components are 3-D printed using nylon material, with the reflector surface, supporting trusses, revolute hinges and spherical hinges combined into single printed parts. Other components include steel pins and ball joint heads. The scale is chosen so that the reflector has a length and width of 660 mm. This model serves to physically validate the deployment process. Figures 18 and 19 show the model with one and two columns respectively. The reflector kinematics are well constrained from full stowage throughout to full deployment. A collision-free single-DOF deployment is observed successfully for both the full two-column reflector, and the single-column variant where components of the second column are removed, confirming inner columns have kinematics independent of outer columns.

The prototype model provides full fidelity for structural details which are not afforded in optimization models. Contact between panels edges can be observed at full deployment. In the prototype model, edges are split perpendicular to the reflector surface and partially chamfered. The reflector surface is designed to be gap-less, so edges touch at full deployment and push against one another. On one hand, contact may cause interference to deployment, and on the other

hand, were guiding geometry features at panel contacts to be added, some desired alignment, structural support, and even latching may be achieved. At smaller scales, especially the plastic prototype model here, such features are more difficult to realize. At larger scales, however, features such as mating surfaces and mechanical latches can be designed to augment reflector performance. A video showing deployment of the full two-layer prototype model is available *.



Fig. 18 Deployed and stowed states of prototype model in the single-layer configuration.



Fig. 19 Deployed and stowed states of prototype model in the full two-layer configuration.

*Prototype deployment video URL: https://youtu.be/v3FzSOnnHWg.

F. Surface error estimation

To estimate the surface precision performance of the proposed reflector in real applications, the effects of manufacturing process uncertainties are considered and quantified. It has been shown that numerical models can accurately predict shape errors and repeatability of deployable structures of various forms [39–41]. A remarkable correlation between a structure's natural vibration frequencies and its surface error resulting from fabrication tolerance is established in [41]. With reflectors where structural properties including stiffness and mass are determined, this is a powerful tool for estimating surface precision. Here, a structure-independent model is pursued, where surface error estimation is to be carried out with only geometric data including panel shapes and truss dimensions. To do so, a truss model is used to represent the reflector structure and capture its deformation. Carrying through from the optimization workflow, truss geometries are generated using origami pattern vertex coordinates and scaled to prototype model size. Additional members are included to represent surface panel supports. As a first estimate and corresponding to prototype model features, all truss members are assigned equal cross section area A and stiffness E. These are algebraic placeholders which are canceled out, thus their numeric values do not affect results. The reflector surface geometry is captured using uniform-mesh-grid point clouds similar to that of the collision model. Point position deviations are calculated from the geometry of the deformed truss. Boundary conditions involve fixed nodes corresponding to the prototype model.

Truss length error is used to represent manufacturing and assembly uncertainties in the reflector components. This provides an equivalent proxy for more complex sources of error, including shape error of components, slop or misalignment of mechanical hinges, as well as deformation from bolt pre-loads etc., and gives insight into the intrinsic structural properties of the reflector. Truss errors are propagated through the structural model to arrive at surface error estimates. The magnification effect of the structure is quantified. This allows upper-bound estimation of RMS surface error based on manufacturing tolerances. RMS surface error can then be used in Ruze's equation [5] to estimate gain for various given RF frequencies. Figure 20 details the process of uncertainty quantification. Each truss is considered to have equal manufacturing uncertainty in its length, independent of nominal truss length. A standard deviation σ_{truss} is assumed for the length of each truss, and its magnification through the structure is evaluated. To evaluate the overall effect caused by all trusses, errors are individually applied to each truss as separate cases, which are considered to have independent probabilities, and the resulting uncertainties are compounded into overall uncertainty values.

For each case, an infinitesimal truss length change δL is applied to a single truss of length L, inducing axial forces of $\frac{AE\delta L}{L}$ and strains of $\frac{\delta L}{L}$. Using a stiffness matrix formulation of the reflector truss, absolute deformation of the truss can be obtained. Absolute deviation of the surface geometry can be calculated using geometric considerations, by evaluating the rotation and translation of truss members to which each surface panel is attached, and applying the spatial transforms to the corresponding point cloud. Note that because δL is small, surface geometry deviation is still assumed to be a linear process under the small-angle approximation. As highlighted in [42], it is distortion not bulk movement

of the surface which most affects reflector RF gain performance, and distortion can be captured by deviation in the surface-normal direction. To evaluate this, a least-squares method is used to fit a spherical surface to the deformed reflector shape. Deviations of the sphere center coordinates and radius can be evaluated, and more importantly the relative surface error of the deformed surface from this best-fit sphere can be evaluated. Here the surface-normal component of deviations is considered. Similar to absolute deviations, relative surface-normal errors are also small and assumed linear. Other surfaces such as paraboloids and hyperboloids can be fitted similarly, provided a correspondingly shaped point cloud is assigned to the reflector geometry model.

Dividing all displacement results by δL gives the linear approximation of expected displacements under unit truss length change. This approximation is valid as long as the small-angle-approximation holds, which is the case for the expected truss length error magnitudes. Considering the structural model as a linear system, the magnitude of displacements are equivalent to expected standard deviations σ_{single} of reflector geometries resulting from unit standard deviation applied at a single truss. After individually evaluating the various deformations and deviations caused by each truss, results including relative surface-normal errors of the reflector surface can be compounded by taking the root-sum-square of standard deviations, where total positional error at each point is $\sigma_{total} = \sqrt{\sum_{all\ trusses} \sigma_{single}^2}$. Finally, the RMS surface error can be obtained by taking the root-mean-square of errors of points in all point clouds representing the reflector surface, where $\sigma_{RMS} = \sqrt{\frac{1}{N_{points}} \sum_{all\ points} \sigma_{total}^2}$.

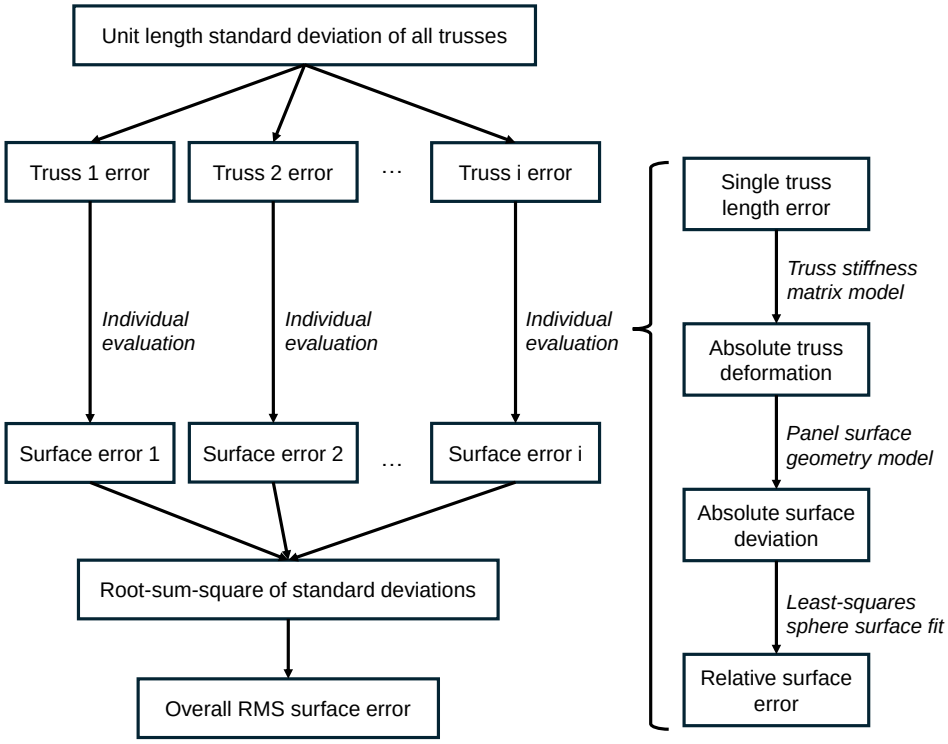
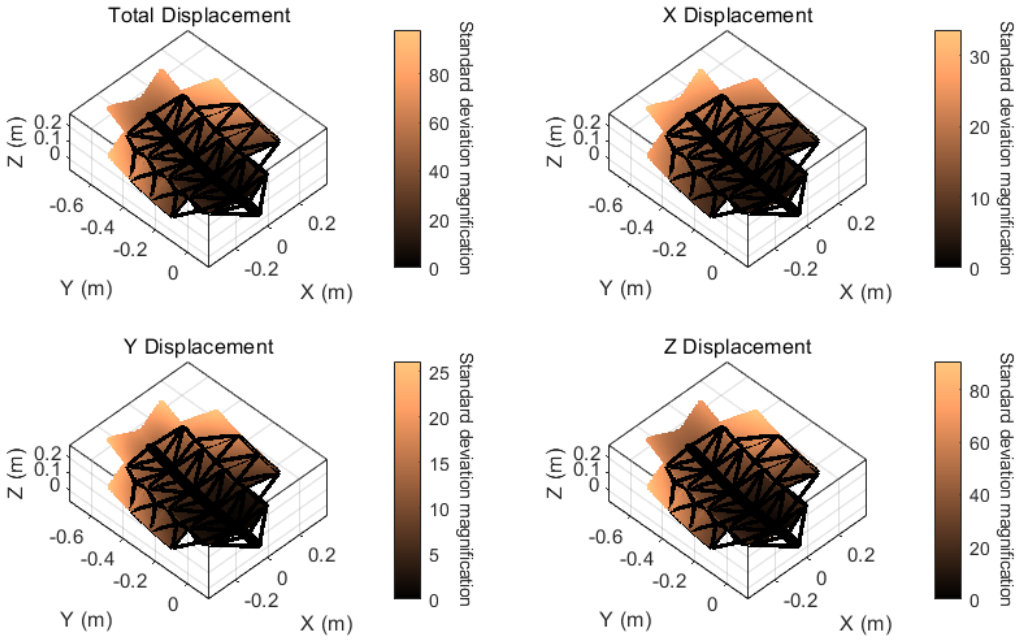
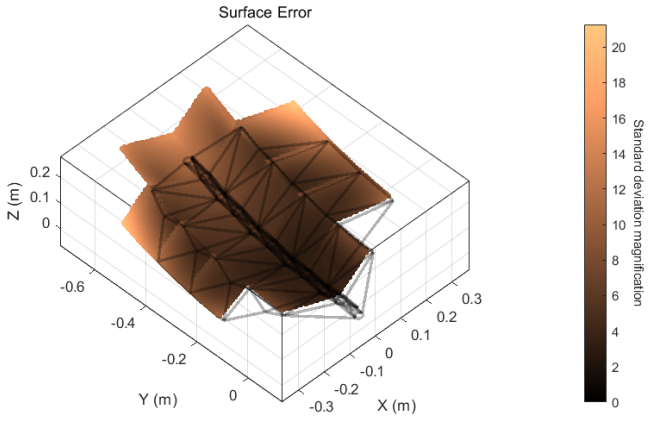


Fig. 20 Methodology for uncertainty propagation.

Figure 21a illustrates the absolute spatial standard deviations of the reflector structure resulting from unit standard deviation applied to every truss in the structure. Total positional uncertainty is magnified up to 98 times that of truss length uncertainties. Figure 21b then shows the relative surface-normal error from a best-fit spherical surface. Surface error is only magnified by up to 21 times, with an RMS value of 7.8 times, as the reflector surface experiences much bulk displacement which does not affect relative surface error. It is noteworthy that the reflector surface panels are assumed to be entirely cantilevered as the most conservative assumption. Surface error distribution reflects this, with panel uncertainties being less severe at panel roots than at tips.



(a) Absolute spatial uncertainty as a magnification of truss uncertainty.



(b) Relative surface normal uncertainty as a magnification of truss uncertainty.

Fig. 21 Uncertainty propagation from truss manufacturing uncertainty.

Table 5 lists the key uncertainty values of reflector geometries. RMS surface error is calculated to be 7.8 times that of truss error. Using this result, truss length tolerances can be translated into surface RMS error tolerances, which represent an upper-bound conservative estimate for surface precision. Errors in sphere center location and radius are magnified more significantly than RMS surface error, but such errors typically at millimeter scale can be easily compensated for by shifting antenna feed position, or be accommodated by antenna feed size.

Overall, such uncertainty values indicate that, under conservative estimates, a 0.02 mm tolerance observed in truss manufacture will correspond to less than 0.16 mm RMS surface error across the reflector surface. With regard to applications, this means manufacturing precision achievable by conventional machining or 3-D printing techniques can support reflector RMS surface errors compatible for as high as V band RF applications, with less than 0.5 dB loss in reflector gain.

Table 5 Key uncertainty values resulting from truss length error.

RMS surface error magnification	7.8×
Sphere center X-component standard deviation magnification	82.9×
Sphere center Y-component standard deviation magnification	131.1×
Sphere center Z-component standard deviation magnification	32.5×
Sphere radius standard deviation magnification	145.9×

The analysis here quantifies how manufacturing uncertainties would affect reflector performance. Using a truss structural model, the magnification effect of the reflector structure from truss length error to surface RMS error is quantified. The structural analysis follows conventional techniques, and linear approximations are used to allow uncertainty propagation. Following the principles of Ruze's equation, surface-normal RMS surface errors are obtained as the key metric which affects reflector RF performance. Further considerations of performance include the effects of gaps, which previous research [43] has studied and provided mitigation techniques for. In addition, the analyses here omit any re-adjustment of surface panels as a conservative evaluation of pure structural performance. The solid-surface truss-supported structure of the proposed reflector readily allows fine adjustments to reduce and eliminate positional errors, which has been shown to significantly improve RMS surface error, both for RF reflectors [44] and optics [2]. Also, being truss supported means the surface panels are not on load paths, and thus can be made into optical mirrors. With precise adjustment techniques, it would be possible to achieve sufficient final surface precision for optical applications.

VII. Conclusion

This paper presents a novel truss-supported doubly-curved deployable reflector which was developed from the Miura-Ori pattern. Key aspects of the work include the following:

- Formulation of a reflector architecture including a supporting truss based on the Miura-Ori pattern, a spine based on the Hoberman linkage, and attached surface panels. The underlying kinematics uniquely achieves single-DOF folding for a doubly-curved Miura-Ori pattern whilst retaining design freedom over the stowed state geometry.
- Systematic parametrization of the reflector geometry and prescription of variables based on design requirements.
- Determination of remaining variables using a kinematics model and a Bayesian optimization approach. Resulting designs display identifiable features which are not tractable through manual design.
- Case study of an example design including optimal geometric parameters, design space examination, detailed mechanical design, derivative variants, manufacture of a prototype model and quantification of surface errors.

The proposed deployable reflector concept is created through a systematic and justifiable design process from the initial architecture to the final prototype. A novel origami-based kinematic architecture provides ample design freedom. A parametric optimization approach is then used to reduce the design problem to a tractable domain, and obtain global optimum. The resulting reflector has a compact shape and a solid surface, and is compatible for multiple scales. Such a Miura-Ori based reflector simultaneously achieves single-DOF deployment, fully-rigid doubly-curved finite-thickness surface panels and supporting trusses, and is a unique design. Potential applications include RF reflectors and optical mirrors for satellites of different scales. In addition, the parametric optimization approach used here is applicable to the design of various structures and mechanisms with complex geometries, while the novel Miura-Ori-based architecture proposed here can also be adapted to a wide range of deployable structures beyond reflectors.

References

[1] Friis, H., "A Note on a Simple Transmission Formula," *Proceedings of the IRE*, Vol. 34, No. 5, 1946, pp. 254–256. https://doi.org/10.1109/JRPROC.1946.234568.

[2] Lightsey, P. A., Atkinson, C. B., Clampin, M. C., and Feinberg, L. D., "James Webb Space Telescope: large deployable cryogenic telescope in space," *Optical Engineering*, Vol. 51, No. 1, 2012, pp. 1 – 20. https://doi.org/10.1117/1.OE.51.1.011003.

[3] Chandra, M., Kumar, S., Chattopadhyaya, S., Chatterjee, S., and Kumar, P., "A review on developments of deployable membrane-based reflector antennas," *Advances in Space Research*, Vol. 68, No. 9, 2021, pp. 3749–3764. https://doi.org/https://doi.org/10.1016/j.asr.2021.06.051.

[4] Ma, X., Li, T., Ma, J., Wang, Z., Shi, C., Zheng, S., Cui, Q., Li, X., Liu, F., Guo, H., Liu, L., Wang, Z., and Li, Y., "Recent Advances in Space-Deployable Structures in China," *Engineering*, Vol. 17, 2022, pp. 207–219. https://doi.org/https://doi.org/10.1016/j.eng.2022.04.013, URL https://www.sciencedirect.com/science/article/pii/S2095809922003642.

[5] Ruze, J., "Antenna tolerance theory—A review," *Proceedings of the IEEE*, Vol. 54, No. 4, 1966, pp. 633–640. https://doi.org/10.1109/PROC.1966.4784.

[6] Kodheli, O., Lagunas, E., Maturo, N., Sharma, S. K., Shankar, B., Montoya, J. F. M., Duncan, J. C. M., Spano, D., Chatzinotas, S., Kisseleff, S., Querol, J., Lei, L., Vu, T. X., and Goussetis, G., "Satellite Communications in the New Space Era: A Survey and Future Challenges," *IEEE Communications Surveys & Tutorials*, Vol. 23, No. 1, 2021, pp. 70–109. https://doi.org/10.1109/COMST.2020.3028247.

[7] Thomson, M., "The AstroMesh deployable reflector," *IEEE Antennas and Propagation Society International Symposium. 1999 Digest. Held in conjunction with: USNC/URSI National Radio Science Meeting (Cat. No.99CH37010)*, Vol. 3, 1999, pp. 1516–1519 vol.3. https://doi.org/10.1109/APS.1999.838231.

[8] Chahat, N., Hodges, R. E., Sauder, J., Thomson, M., Peral, E., and Rahmat-Samii, Y., "CubeSat Deployable Ka-Band Mesh Reflector Antenna Development for Earth Science Missions," *IEEE Transactions on Antennas and Propagation*, Vol. 64, No. 6, 2016, pp. 2083–2093. https://doi.org/10.1109/TAP.2016.2546306.

[9] Guest, S., and Pellegrino, S., "A new concept for solid surface deployable antennas," *Acta Astronautica*, Vol. 38, No. 2, 1996, pp. 103–113. https://doi.org/https://doi.org/10.1016/0094-5765(96)00009-4.

[10] Imbriale, W. A., (Shichang), S., and Boccia, G. L., *Space Antenna Handbook*, 1st ed., John Wiley & Sons, Ltd, Chichester, 2012, Chap. 16, p. 658.

[11] Schwarz, S., and Barho, R., "Deployment Mechanisms for a 5m Unfurlable Reflector," *Proc. 18. European Space Mechanisms and Tribology Symposium*, 2019, pp. 1–7. Munich, Germany.

[12] Dufour, L., Datashvili, L. S., Guinot, F., Legay, H., and Goussetis, G., "Origami Deployable Reflector Antenna for CubeSats," *AIAA Scitech 2021 Forum*, 2021, pp. 1–15. https://doi.org/10.2514/6.2021-1703, URL https://arc.aiaa.org/doi/abs/10.2514/6.2021-1703.

[13] Footdale, J. N., and Banik, J., "System Design Study of a Deployable Reflector Antenna with Flexible Shell Segments," *3rd AIAA Spacecraft Structures Conference*, 2016, pp. 1–11. https://doi.org/10.2514/6.2016-0698.

[14] Ikeya, K., Sakamoto, H., Nakanishi, H., Furuya, H., Tomura, T., Ide, R., Iijima, R., Iwasaki, Y., Ohno, K., Omoto, K., Furuya, T., Hayashi, T., Kato, M., Koide, S., Kurosaki, M., Nakatsuka, Y., Okuyama, S., Kashiyama, R., Nakamura, J., Nio, W., Tsunemitsu, T., Yamazaki, Y., Taga, K., Hohmann, B., Amamoto, T., Chubachi, T., Tamura, S., Okada, H., Watanabe, A., Kawabata, N., Hori, T., Ito, H., Kuratomi, T., Shimoda, Y., Hidaka, N., Watanabe, K., Torisaka, A., and Yamazaki, M., "Significance of 3U CubeSat OrigamiSat-1 for space demonstration of multifunctional deployable membrane," *Acta Astronautica*, Vol. 173, 2020, pp. 363–377. https://doi.org/https://doi.org/10.1016/j.actaastro.2020.04.016, URL https://www.sciencedirect.com/science/article/pii/S0094576520302204.

[15] Wang, T., and Santer, M. J., "An Origami-Based Rigid-Foldable Parabolic Reflector Concept," *AIAA SCITECH 2022 Forum*, 2022, pp. 1–18. https://doi.org/10.2514/6.2022-1885.

[16] Wang, T., and Santer, M. J., "Design and Prototyping of an Origami-Based Rigid-Foldable Parabolic Reflector," *AIAA SCITECH 2023 Forum*, 2023, pp. 1–14. https://doi.org/10.2514/6.2023-0755.

[17] Wang, T., and Santer, M., "Rigid-Foldable Parabolic Deployable Reflector Concept Based on the Origami Flasher Pattern," *Journal of Spacecraft and Rockets*, 2023. https://doi.org/10.2514/1.A35497.

[18] Wang, T., and Santer, M. J., "A Truss-Supported Doubly-Curved Deployable Reflector Based on the Miura-Ori Pattern," *AIAA SCITECH 2024 Forum*, 2024, pp. 1–18. https://doi.org/10.2514/6.2024-2256.

[19] Guest, S. D., "Deployable Structures: Concepts and Analysis," Ph.D. thesis, University of Cambridge Corpus Christi College, Cambridge UK, 1994.

[20] Russo, A., Barakali, B., Kitsu, K. I., Baudet, L., Yang, J., and Zhong, Y., "Origami-inspired self-deployable reflectarray antenna," *Acta Astronautica*, Vol. 213, 2023, pp. 240–251. https://doi.org/https://doi.org/10.1016/j.actaastro.2023.08.007, URL https://www.sciencedirect.com/science/article/pii/S0094576523004058.

[21] Robb, B., Russo, A., Soldini, S., Paoletti, P., Reveles, J., Bailet, G., and McInnes, C. R., "Integrated attitude and shape control for OrigamiSats with variable surface reflectivity," *Acta Astronautica*, Vol. 211, 2023, pp. 393–404. https://doi.org/https://doi.org/10.1016/j.actaastro.2023.06.025, URL https://www.sciencedirect.com/science/article/pii/S0094576523003259.

[22] Kuriki, K., Ninomiya, K., Takei, M., and Matsuoka, S., "Lessons learned from the space flyer unit (SFU) mission," *Acta Astronautica*, Vol. 51, No. 11, 2002, pp. 797–806. https://doi.org/https://doi.org/10.1016/S0094-5765(02)00026-7.

[23] Walker, A., and Stankovic, T., "Algorithmic design of origami mechanisms and tessellations," *Communications Materials*, Vol. 3, No. 1, 2022, p. 4. https://doi.org/10.1038/s43246-022-00227-5.

[24] Dudte, L. H., Vouga, E., Tachi, T., and Mahadevan, L., "Programming curvature using origami tessellations," *Nature Materials*, Vol. 15, No. 5, 2016, pp. 583–588. https://doi.org/10.1038/nmat4540.

[25] Tachi, T., "Generalization of rigid foldable quadrilateral mesh origami," *Journal- International Association for Shell and Spatial Structures*, Vol. 50, 2009, pp. 173–179.

[26] Hu, Y., Zhou, Y., and Liang, H., "Constructing Rigid-Foldable Generalized Miura-Ori Tessellations for Curved Surfaces," *Journal of Mechanisms and Robotics*, Vol. 13, No. 1, 2020. https://doi.org/10.1115/1.4048630.

[27] Pruett, H. T., Kaddour, A.-S., Georgakopoulos, S. V., Howell, L. L., and Magleby, S. P., "Optimizing geometry for EM performance to design volume-efficient Miura-ori for reflectarray antennas," *Extreme Mechanics Letters*, Vol. 56, 2022, p. 101889. https://doi.org/https://doi.org/10.1016/j.eml.2022.101889.

[28] Yu, H., Guo, Z., and Wang, J., "A method of calculating the degree of freedom of foldable plate rigid origami with adjacency matrix," *Advances in Mechanical Engineering*, Vol. 10, No. 6, 2018, p. 1687814018779696. https://doi.org/10.1177/1687814018779696, URL https://doi.org/10.1177/1687814018779696.

[29] Hoberman, C., "Reversibly expandable doubly-curved truss structure," , Jul 1990. US Patent 4942700A.

[30] You, Z., and Pellegrino, S., "Foldable bar structures," *International Journal of Solids and Structures*, Vol. 34, No. 15, 1997, pp. 1825–1847. https://doi.org/https://doi.org/10.1016/S0020-7683(96)00125-4.

[31] Rogers, C. A., Stutzman, W. L., Campbell, T. G., and Hedgepeth, J. M., "Technology Assessment and Development of Large Deployable Antennas," *Journal of Aerospace Engineering*, Vol. 6, No. 1, 1993, pp. 34–54. https://doi.org/doi:10.1061/(ASCE)0893-1321(1993)6:1(34), URL https://ascelibrary.org/doi/abs/10.1061/%28ASCE%290893-1321%281993%296%3A1%2834%29.

[32] Hedgepeth, J. M., "Structrures for Remotely Deployable Precision Antennas," *NASA Contractor Report*, 1989.

[33] FreeFall-Aerospace, "Antennas: Communications Infrastructure for Earth and Cislunar Solutions," , Sep 2023. URL https://www.freefallaerospace.com/antennas/.

[34] Chandra, A., Pat, T., Tonazzi, J. C. L., and Walker, C. K., "Development and flight qualification of a small satellite X-band spherical membrane antenna," *2021 IEEE Aerospace Conference (50100)*, 2021, pp. 1–8. https://doi.org/10.1109/AERO50100.2021.9438525.

[35] Korsawe, J., "Minimal bounding box," , 2015. URL https://uk.mathworks.com/matlabcentral/fileexchange/18264-minimal-bounding-box.

[36] MathWorks, *MATLAB*, R2023a. URL https://www.mathworks.com/products/matlab.html.

[37] MathWorks, "Kernel (Covariance) Function Options," , 2023. URL https://uk.mathworks.com/help/stats/kernel-covariance-function-options.html.

[38] Rasmussen, C. E., and Williams, C. K. I., *Gaussian Processes for Machine Learning*, The MIT Press, 2005. https://doi.org/10.7551/mitpress/3206.001.0001, URL https://doi.org/10.7551/mitpress/3206.001.0001.

[39] Antoun, G., Ferraro, S., McDonell, R., Bradford, S. C., and Arya, M., "A Validated Numerical Model of Deployment Accuracy and Repeatability of the Starshade Inner Disk Subsystem," *AIAA SCITECH 2024 Forum*, 2024, pp. 1–26. https://doi.org/10.2514/6.2024-2254, URL https://arc.aiaa.org/doi/abs/10.2514/6.2024-2254.

[40] San, B., Yang, Q., and Yin, L., "Stochastic and sensitivity analysis of shape error of inflatable antenna reflectors," *Acta Astronautica*, Vol. 132, 2017, pp. 170–176. https://doi.org/https://doi.org/10.1016/j.actaastro.2016.12.015, URL https://www.sciencedirect.com/science/article/pii/S009457651630460X.

[41] Hedgepeth, J. M., "Influence of fabrication tolerances on the surface accuracy of largeantenna structures," *AIAA Journal*, Vol. 20, No. 5, 1982, pp. 680–686. https://doi.org/10.2514/3.7936, URL https://doi.org/10.2514/3.7936.

[42] Li, S., Fan, Y., and Chen, Q., "Surface Error Distribution Research in Reflector Antenna from the Measured Data," *Journal of Spacecraft and Rockets*, Vol. 58, No. 2, 2021, pp. 589–594. https://doi.org/10.2514/1.A34826, URL https://doi.org/10.2514/1.A34826.

[43] Hüschelrath, J., "The electromagnetic problem of interpanel gaps in reflector antennas," *Acta Astronautica*, Vol. 57, No. 2, 2005, pp. 356–371. https://doi.org/https://doi.org/10.1016/j.actaastro.2005.03.022, URL https://www.sciencedirect.com/science/article/pii/S0094576505001177.

[44] Yao, Z., Wu, T., Zhou, Y., and Fang, H., "Surface Accuracy Study for a Segmented Reflector," *AIAA Scitech 2019 Forum*, 2019, pp. 1–12. https://doi.org/10.2514/6.2019-0753, URL https://arc.aiaa.org/doi/abs/10.2514/6.2019-0753.